Preprint
UCRL-JC-135131

Analysis, Comparison and Modeling of Radar Interferometry Data of Surface Deformation Signals Associated with Underground Explosions, Mine Collapses and Earthquakes. Phase 1: Underground Explosions, Nevada Test Site

P. Vincent, B. Foxall, W.R. Walter

This paper was prepared for submittal to the 21st Seismic Research Symposium: Technologies for Monitoring the Comprehensive Nuclear Test-Ban-Treaty, Las Vegas, NV, September 21-24, 1999

U.S. Department of Energy
Lawrence Livermore National Laboratory

July 23, 1999

ANALYSIS, COMPARISON AND MODELING OF RADAR INTERFEROMETRY DATA OF SURFACE DEFORMATION SIGNALS ASSOCIATED WITH UNDERGROUND EXPLOSIONS, MINE COLLAPSES AND EARTHQUAKES

PHASE 1: UNDERGROUND EXPLOSIONS, NEVADA TEST SITE

Paul Vincent, Bill Foxall and William R. Walter

Geophysics and Global Security Division
Lawrence Livermore National Laboratory

Sponsored by U.S. Department of Energy
Office of Non-Proliferation and National Security
Office of Research and Development

Contract No. W-7405-ENG-48

ABSTRACT

We have previously presented simple elastic deformation modeling results for three classes of seismic events of concern in monitoring the CTBT – underground explosions, mine collapses and earthquakes. Those results explored the theoretical detectability of each event type using synthetic aperture radar interferometry (InSAR) based on commercially available satellite data. In those studies we identified and compared the characteristics of synthetic interferograms that distinguish each event type, as well the ability of the interferograms to constrain source parameters. These idealized modeling results, together with preliminary analysis of InSAR data for the 1995 m_b5.2 Solvay mine collapse in southwestern Wyoming, suggested that InSAR data used in conjunction with regional seismic monitoring holds great potential for CTBT discrimination and seismic source analysis, as well as providing accurate ground truth parameters for regional calibration events.

In this paper we further examine the detectability and "discriminating" power of InSAR by presenting results from InSAR data processing, analysis and modeling of the surface deformation signals associated with underground explosions. Specifically, we present results of a detailed study of coseismic and postseismic surface deformation signals associated with underground nuclear and chemical explosion tests at the Nevada Test Site (NTS). Several interferograms were formed from raw ERS-1/2 radar data covering different time spans and epochs beginning just prior to the last U.S. nuclear tests in 1992 and ending in 1996. These interferograms have yielded information about the nature and duration of the source processes that produced the surface deformations associated with these events. A critical result of this study is that significant post-event surface deformation associated with underground nuclear explosions detonated at depths in excess of 600 meters can be detected using differential radar interferometry. An immediate implication of this finding is that underground nuclear explosions may not need to be "captured" coseismically by radar images acquired before and after an event in order to be detectable. This has obvious advantages in CTBT monitoring since suspect seismic events-which usually can be located within a 100 km by 100 km area of an ERS-1/2 satellite frame by established seismic methods-can be imaged after the event has been identified and located by existing regional seismic networks.

Key Words: InSAR, SLC images, interferogram, synthetic interferogram, ERS-1/2 frame, phase unwrapping, DEM, coseismic, postseismic, source parameters.

This work is performed under the auspices of the U.S. Department of Energy by the Lawrence Livermore National Laboratory under contract W-7405-ENG-48.

Introduction

Synthetic aperture radar interferometry (InSAR) is rapidly becoming a new standard geodetic technique to map surface deformation signals from a variety of sources. InSAR is capable of mapping sub-centimeter vertical deformation signals over a 100 x 100 km area and has a resolution (pixel size) of about 20 meters. Although most applications published to date have been to high-rate deformation fields over short time periods, it has recently been shown that low-rate deformation fields can be imaged over time periods in excess of 4.5 years depending on orbital baseline distances, vegetation cover and the climate of the region imaged [Rosen, et al, 1997, Vincent, et al, 1997, Vincent, 1998]. As part of an effort to determine whether InSAR can be used to help discriminate between different types of seismic events, we previously showed that the expected signals from the simplest elastic models of three source types (mine collapses, explosions and small, shallow earthquakes) give very different expected surface deformation signals [Foxall et al, 1998]. In order to better understand the surface deformation produced by underground explosions, we investigate in this paper actual surface deformation signals associated with underground nuclear and chemical explosion tests at the Nevada Test Site. These surface deformations were imaged by processing raw ERS-1/2 satellite data collected over the site from 1992 through 1996 (see Figure 1) and creating deformation maps.

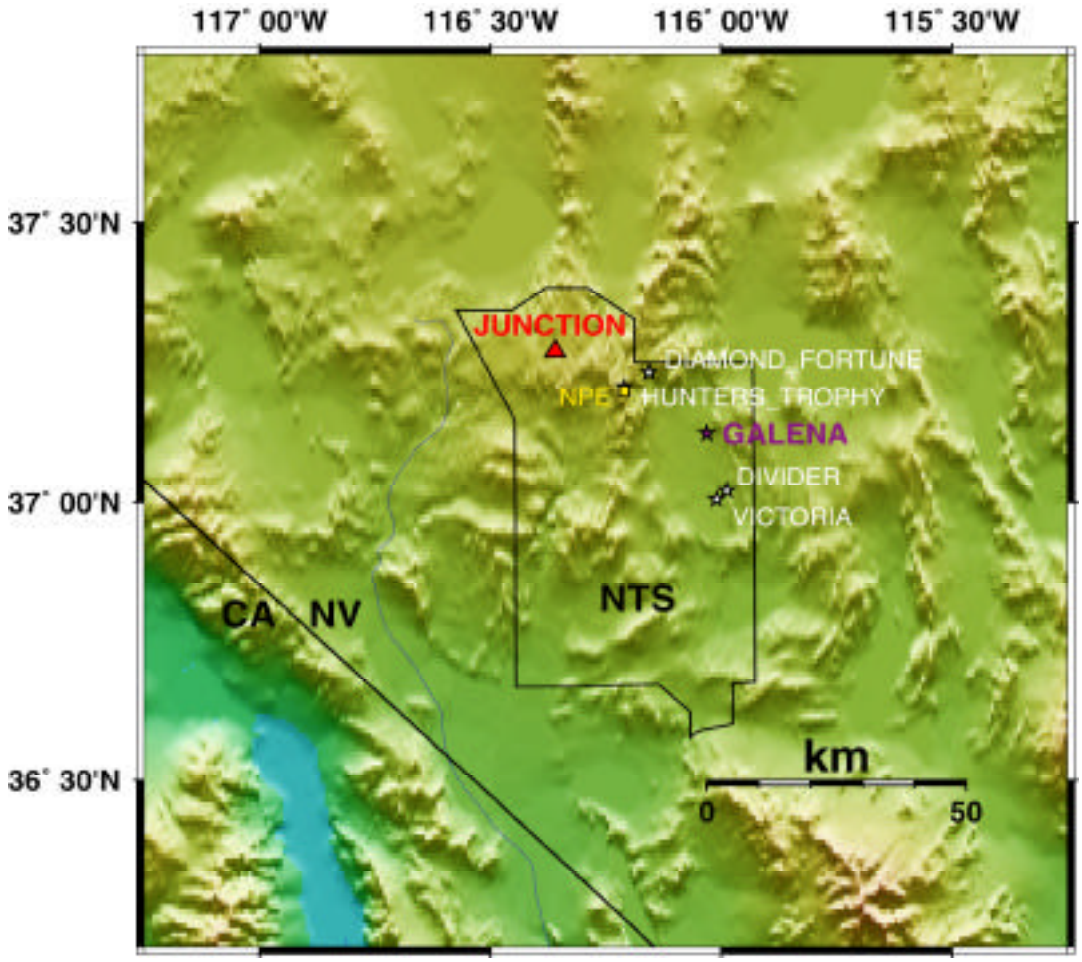

Figure 1. Shaded relief map of the Nevada Test Site showing the location of underground nuclear tests from April 1992 to the last test done in September 1992 (stars). Also shown are the Non-Proliferation Experiment (NPE) a large underground chemical test (square), and JUNCTION the last large Pahute Mesa underground nuclear test done in March 1992 (triangle). Of all the explosions shown, only GALENA produced a surface crater.

Differential InSAR Method

Figure 2 shows the basic imaging geometry of three repeat orbit passes imaging the same region on the ground. The first (reference) satellite position is denoted by A_1 and the second (repeat) orbit position is denoted A_2 (orbit direction is into the page). The relative distance between the two satellite positions at their respective scene acquisition times is referred to as the orbital baseline B. The baseline can be decomposed into perpendicular and parallel components—the parallel component is the relative satellite separation toward or away from the ground parallel to the satellite-to-ground or line-of-sight (los) vector and the perpendicular component is the relative satellite separation perpendicular to this direction. It is the perpendicular component of the baseline that determines the degree of parallax between the two imaging positions and hence the fringe rate—the larger this separation the higher the interference fringe rate will be in a resulting interferogram. When the phase value of each ground pixel viewed from two repeat orbit positions are combined interferometrically and subtracted, the resulting phase values or fringes are proportional to the topography of the ground region imaged. This is because the phase is proportional to the round trip distance between a ground point (pixel) and the imaging satellite—topographic highs will have a lower phase value then topographic lows. If any ground deformation occurs between the repeat orbits, then the phase will be proportional to the sum of the topographic phase signature plus a deformation phase signature. To isolate the desired deformation phase signature the topographic phase must be removed. This can be accomplished in one of two ways. One way is to construct another interferogram using another orbit pair imaging the same ground frame but with minimal time between scene acquisitions to minimize the possibility of any ground deformation occurring between orbit passes. The phase from this second interferogram will be proportional to the topography only and this can be resampled to the first (deformation) pair to remove the topographic phase from the first orbit pair. The second way to do this is to simulate a Digital Elevation Map (DEM) into the radar coordinates of the first (deformation) pair and subtract the simulated topographic phase from the deformation pair to remove topographic phase. Both these methods are referred to as *differential* interferometry. Figure 2 depicts the "3-pass" method whereby a second topography pair is formed by sharing one common orbit with the first pair (A_1-A_2'). Once the topographic phase is removed, the remaining fringes will be proportional to the ground surface deformation plus any atmospheric artifacts and other noise sources. Typically, atmospheric noise terms (both tropospheric and ionospheric noise sources) have a recognizable signature and can usually be isolated from small concentrated deformation signals similar to those seen in this study [e.g., see Massonnet and Feigl, 1998; Vincent, 1998].

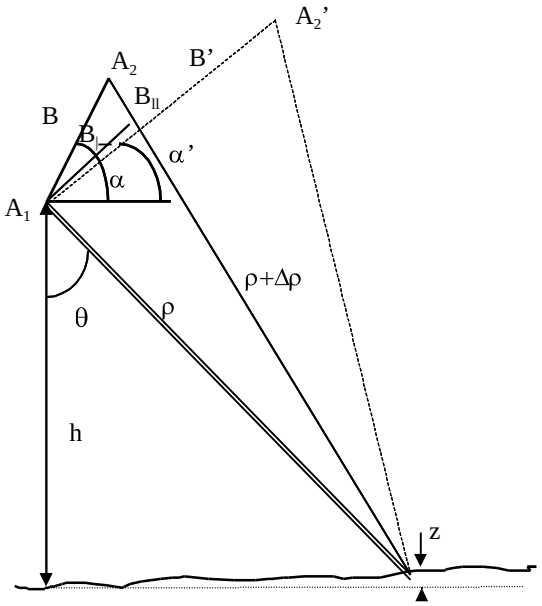

Figure 2. Radar imaging geometry. The solid lines show line-of-sight (los) vectors for the first interferometric pair formed by satellite positions at A_1 and A_2. Dashed lines show paths for a second interferometric pair (A_1-A_2') used to remove topographic phase from the first. Parallel and perpendicular components of the orbital baseline are shown. Path of satellite is into the page.

Data Selection

The ERS data chosen for this study are shown in Table 1. The pairs were chosen based on two criteria. The first was to obtain pairs which had the minimum perpendicular baseline component available (to minimize temporal decorrelation) and the second was to obtain orbit pairs of different time spans and epochs in order to capture both co-event and post-event signals as well as short and long-term deformation signals. Table 2 lists the interferometric orbit pairs of data from Table 1, along with relevant interferometry parameters described above. The ambiguity height is the amount of topographic change across the image required to produce the observed fringe rate seen in a deformation interferogram where topography either has not been removed or it has been removed imperfectly leaving residual topographic fringes. The larger this number, which is inversely proportional to the perpendicular baseline component, the less ambiguous the phase signal is between representing topography and representing change in topography with time (i.e., deformation).

Table 1. Raw ERS SAR data acquired for Nevada Test Site Study

Image #	Satellite—Orbit	Frame	Acquisition Date
1	ERS-1 --4051	2853	Apr 24, 1992
2	ERS-1 –8560	“	Mar 5, 1993
3	ERS-1 –10063	“	Jun 18, 1993
4	ERS-1 –20427	“	Jun 11, 1995
5	ERS-1 –25437	“	May 26, 1996

Table 2. InSAR orbit pairs formed and relevant parameters

Image Pair	Sensors	Epoch	Time Span	Perp. Baseline	Ambig. Height
1/2	ERS-1	920424-930305	315 days	50m	184m
1/3	ERS-1	920424-930618	420 days	41m	224m
3/4	ERS-1	930618-950611	723 days	66m	139m
1/5	ERS-1	920424-960526	1492 days	20m	462m

Raw Data Processing

All of the SAR data listed in Table 1 represents raw unprocessed data. These data sets were processed using the Jet Propulsion Laboratory (JPL) IntSoft software suite. The raw data were processed to zero (compensated) Doppler, slant range projection, phase-preserved single-look complex (SLC) images. These focused images have pixel dimensions (resolution) of about 20m in ground range (cross-track direction) by 22.5m in azimuth (along-track direction). The SLC images are paired according to favorable (smallest) orbital baselines to form the interferograms.

InSAR Processing

The second SLC image in each interferometric pair (shown in Table 2) was coregistered and resampled to the first to sub-pixel precision and the phase difference was computed to form the raw interferogram. The raw interferograms were then “flattened” by removing orbital and earth curvature phase artifacts from the raw interferograms. The phase in the interferograms are modulo 2π and must be unwrapped to obtain absolute phase values. The phase was unwrapped using the residue-branch cut method of phase integration by [Goldstein, et al., 1988]. The unwrapped phase was then converted to range change using an average ERS-1/2 incidence (look angle) of 23 degrees from vertical.

Topographic phase was removed from the interferograms by constructing a Digital Elevation Map (DEM) using U.S. Geological Survey 1 degree (83 meter pixel size resolution) DEMs covering the imaged frame. DEMs ‘goldfield-e’, ‘caliente-w’, ‘death_valley-e’, and ‘las_vegas-w’ were mosaiced and cropped to overlay the ERS image frame centered over the Nevada Test Site.

Results and Analysis

Figure 3 shows the radar amplitude image of the study area. The boxes enclose the locations of events JUNCTION (920326-- Pahute Mesa) and GALENA (920623-- Pahute Mesa). Deformation maps of the boxed areas are shown in Figures 4-6. Figure 4 shows the four deformation maps derived from the four interferograms of the boxed areas around event JUNCTION. Figure 5 shows profile plots done along the major and minor axis of the deformation signal associated with JUNCTION captured in orbit pair 1/3 (920424-930618). Figure 6 shows the map and W-E profile plot of the coseismic (i.e., captured by before and after-event orbit passes) deformation signal produced by event GALENA, which formed a crater.

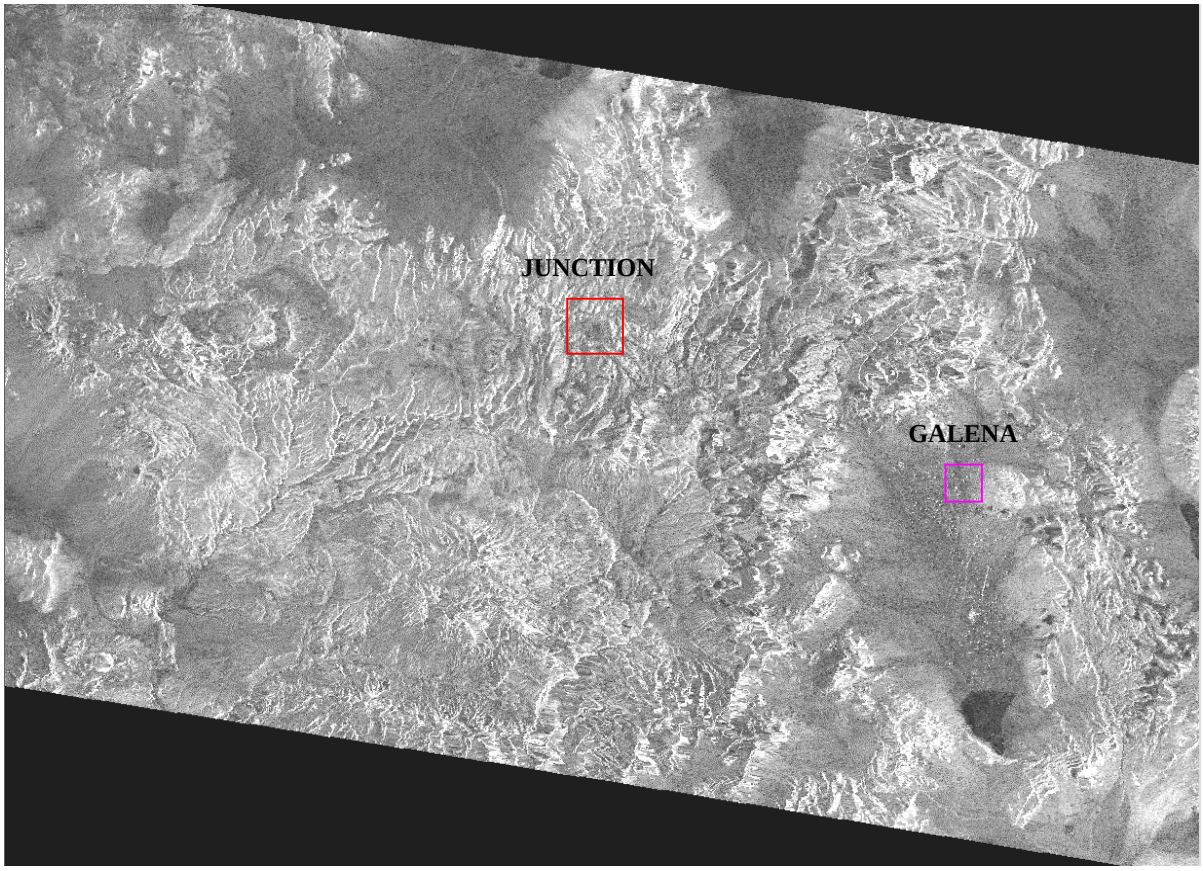

Figure 3. Geocoded radar amplitude image of ERS frame 2853 centered over the Nevada Test Site. Red box shows the location of event JUNCTION , the last large Pahute Mesa test, and the purple box shows the location of event GALENA.

JUNCTION

The interferogram/deformation map for image pair 1/2 (920424-930305) is mostly decorrelated in the higher mountainous regions of the imaged frame. This is most likely due to winter weather (possibly snow cover in the highest elevations in the image) contaminating the radar reflectivity function of orbit 8560 which was acquired in mid-winter (930305). This can be deduced from the fact that image pair 1/3 (acquired in spring and summer months) which has image #1 in common with image pair 1/2, has excellent correlation, has a comparable orbital baseline and a longer temporal baseline. Image pair 1/3 shows post-JUNCTION event deformation since the date of the first orbit in that pair (920424) post-dates the JUNCTION event (920326) by one month. Image pair 3/4 shows a notable *absence* of any deformation signal over the JUNCTION test location. This observation puts an upper bound on the duration of the post-seismic signal associated with JUNCTION of 420 days. The postseismic deformation

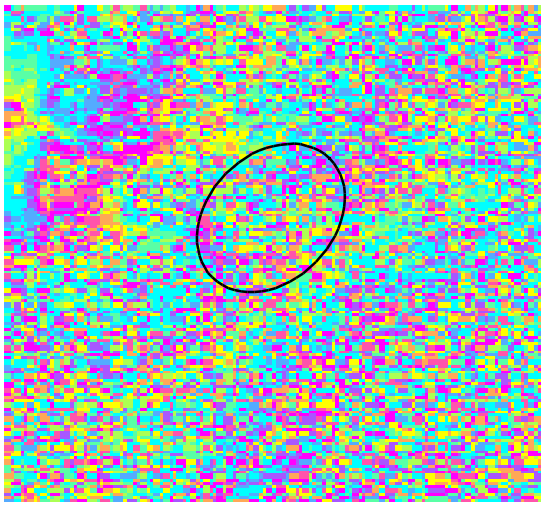

orbit pair 1/2 (920424-930305)

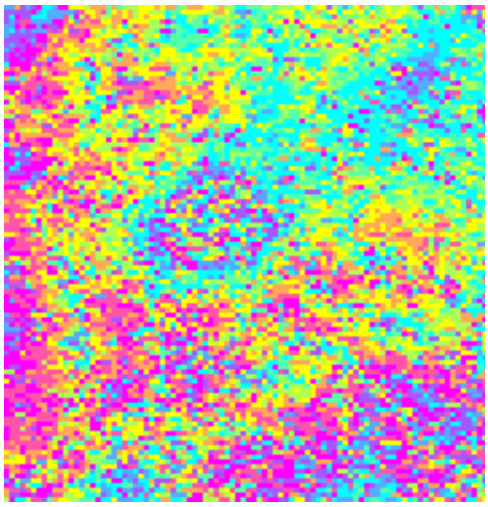

orbit pair 1/5 (920424-960526)

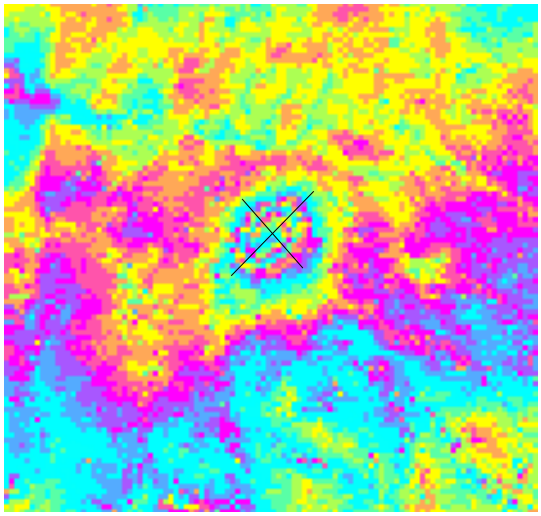

orbit pair 1/3 (920424-930618)

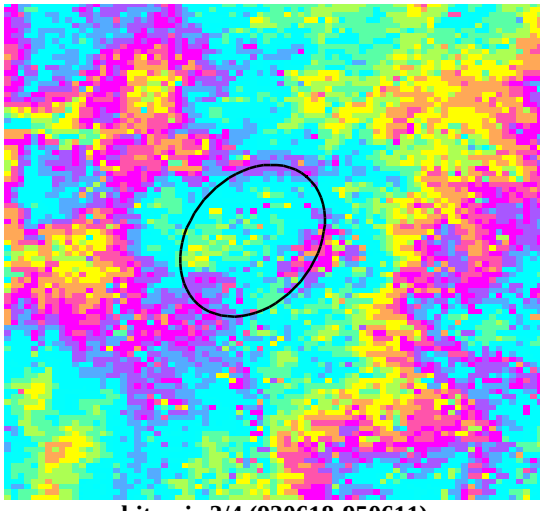

orbit pair 3/4 (930618-950611)

Figure 4. Deformation maps showing post-seismic surface deformation signals collocated with the JUNCTION nuclear test of March 26, 1992 (red box shown in Figure 3). Counterclockwise from upper left corner: orbit pair 1/2, 920424-930305 (mostly decorrelated); orbit pair 1/3, 920424-930618 (post-seismic signal clearly visible); orbit pair 3/4, 930618-950611 (no deformation signal visible); orbit pair 1/5, 920424-960526 (post-seismic signal visible but degraded by temporal decorrelation). Upper bound on duration of post-seismic deformation signal associated with the Junction event is 420 days (most likely less—see text). Cross-hairs denote profile locations for major and minor axis of deformation ellipse signal. shown in Figure 5. Black ellipses show the corresponding location of the JUNCTION signal in each deformation map where no signal is detected.

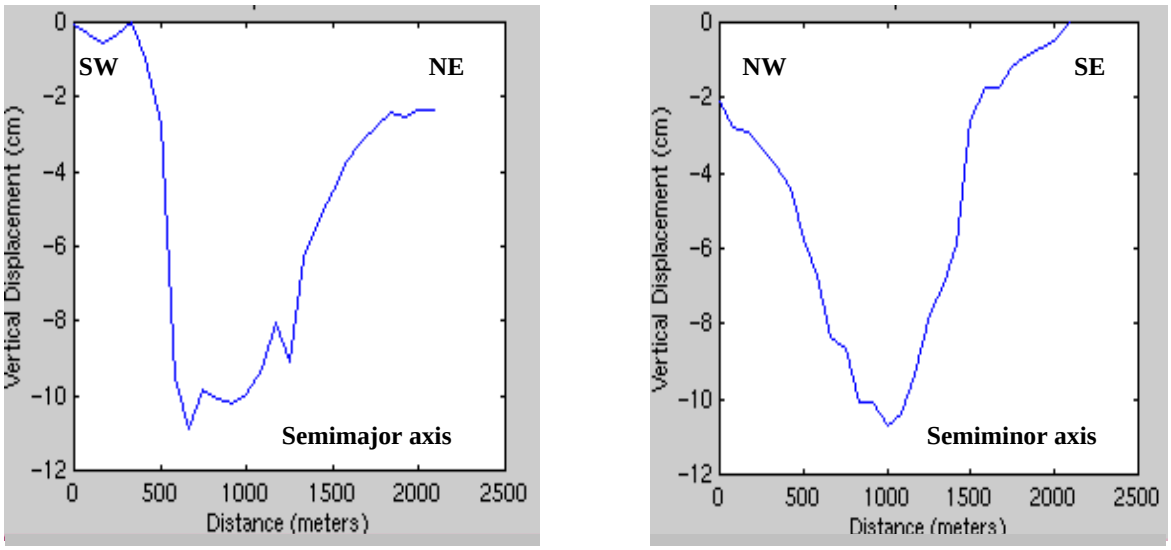

Figure 5. Profiles along major (left) and minor (right) axis of elliptical post-seismic deformation pattern above the JUNCTION test site location (see text).

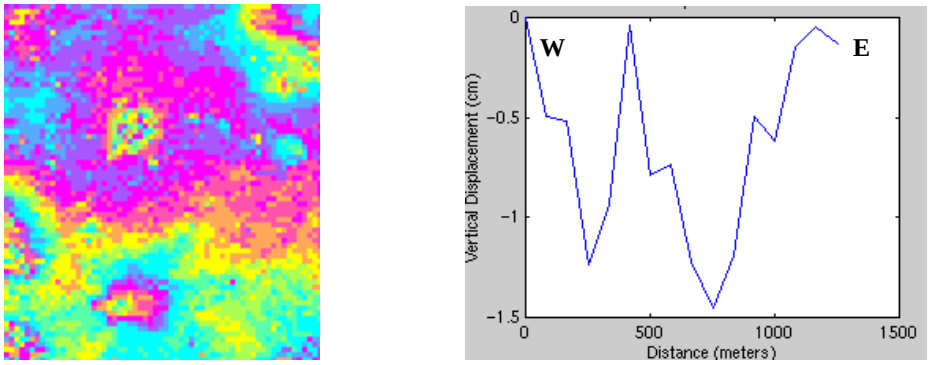

Figure 6. Deformation map (left) and profile across west to east (right) of coseismic deformation associated with the GALENA nuclear test of June 23, 1992 (purple box shown in Figure 3). Image is from orbit pair 1/2 (920424-930305). [Note: Event GALENA is the only event shown in Figure 2 that cratered and shows no significant post-seismic deformation signal in any of the interferograms shown.

signal seen in image pair 1/5 is remarkably similar to that in image pair 1/3, which also suggests that the post-seismic signal is limited in duration to less than 420 days after the event. The relatively long time baseline of this pair (1492 days) is the reason for the increased decorrelation compared to image pair 1/3. Black ellipses are drawn over the same region in each deformation map to show the location of the JUNCTION event in each map. Profiles were done across the major and minor axes of the deformation ellipse visible in image pair 1/3 (shown in Figure 5 above) and show approximately 10 centimeters of subsidence during the 420 days between images. It is not known whether this subsidence signal occurred over a shorter period but we suspect so and plan to purchase additional orbit pairs to further constrain both the duration and timing of this signal. Both profile plots across the deformation signal show an apparent diameter of about 2 km. The profile taken from SW to NE (the major axis) shows an approximately 800 meter flattened center, while the profile taken from NW to SE does not show a flattened center region. In addition, the outer region of the strain ellipse is tilted down slightly to the north as can by seen on the northeast and northwest ends of the profile plots. The center region, however, has a subtle *relative* uplifted flank on

the northern interior of the strain ellipse. This asymmetry suggests a complicated deformation source for the observed signal.

GALENA

Figure 6 shows image pair 1/2 which captures a coseismic deformation signal over event GALENA (see Figures 2 and 3). GALENA formed a coseismic crater 134 meters in diameter and 8 meters deep 17 minutes after the test [LLNL Containment Data Base]. The W-E profile across this feature from (Figure 6) shows two abrupt subsidence regions separated by an (offset) central peak of near-zero net deformation. It is important to note that the profile shown in Figure 6 (as well as other similar profiles done of this feature) does not accurately measure actual crater formation, but instead captures the peripheral deformation of the ground immediately surrounding the crater. The reason for this is that the relatively small radius and large magnitude of the actual cratering event prevent coherent detection and measurement by C-band (5.6 cm wavelength) InSAR methods. Other "stereo" interferometric techniques whereby high resolution inteferometric topographic images before and after an event can be combined stereoscopically to image this type of large deformation signal [Jackowitz, 1999, personal communication].

Source Characterization and Modeling

The majority of NTS events produce either a crater or immediate post-shot (generally minutes to days) subsurface collapse regardless of whether the shot is detonated within alluvium, tuff or rhyolite lava. The post-shot data [W. Brunish, LANL, personal communication] indicate that JUNCTION caused a subsurface collapse up to a depth of about 300m approximately 29 hours after detonation. In general, the dominant post-shot collapse mechanism is chimneying, in which the explosion cavity void migrates upwards as blocks of fractured rock fall to fill in the cavity below. A crater is formed if the chimney reaches the free surface. The volume of the domed 'apical' cavity above the chimney will, in general, decrease as the chimney propagates upward, since chimneying creates pore volume due to mismatch between the fallen blocks of rock, a process referred to as 'bulking'. Chimneying usually takes place over the span of a few seconds.

There are several possible mechanisms for delayed or continued subsidence of like that imaged by the InSAR data following the main collapse. These include: (1) Either abrupt or slow closure of the chimney apical void, including settlement of chimney rubble; (2) gravitational settlement of a possibly larger detached (uplifted) zone possibly from spall; and (3) dip-slip on nearby faults reactivated by the shot or post-shot movement. We carried out preliminary elastic modeling to investigate mechanism (1) as a possible source of the subsidence imaged by the InSAR data. Apical cavity closure was modeled as a closing rectangular horizontal tension crack centered at 300 m in an elastic half-space having Poisson ratio and rigidity of 0.3 and 2.3×10^9 Pa, respectively (representative of the overburden of Pahute Mesa). Dislocation dimensions ranged from 120m to 180m; this is estimated to be a reasonable range of for the width of the chimney at 300m depth based on an explosion cavity radius of 60m estimated from the m_b vs yield relationship of Murphy [1996] together with the scaled cavity radius vs. overburden pressure curves of Terhune and Glenn [1977]. All of the apical cavity models produced calculated surface subsidence troughs that are too narrow to fit the observations (Fig. 5). A closing crack model at a depth of about 600m, close to the source point, with a displacement of about 5m is required to produce even a reasonable fit to the magnitude of the subsidence signal but does not reproduce its elliptical shape. This possibility appears to be precluded, in any case, by the main post-shot collapse.

We also carried out preliminary elastic modeling to investigate mechanism (2) as a possible source. The best-fit model in this case is a 12 centimeter dislocation on a 300 meter deep closing horizontal crack with dimensions 800 meters wide by 1100 meters long oriented N40E. Figure 7 shows profile plots for the data and synthetic interferograms along the major and minor axis of the deformation signal . This model fits both the overall magnitude and the orientation of the elliptical signal but does not reproduce the asymmetry and steep gradients seen in the interferogram. The steep northern side and flat bottom of the trough in the NE-SW (major axis) profile suggests that part of the subsidence might be associated with a down-dropped block between two faults. We are continuing to investigate these and the other possible mechanisms. The elliptical shape and orientation of the subsidence imaged by InSAR are consistent with the results reported by Ellis and Snyder [1974]. These authors showed that the majority of shots in bedrock under Yucca Flats form craters having ellipticities of 1.1 or greater and major axes preferentially oriented within the range N50E-N70E.

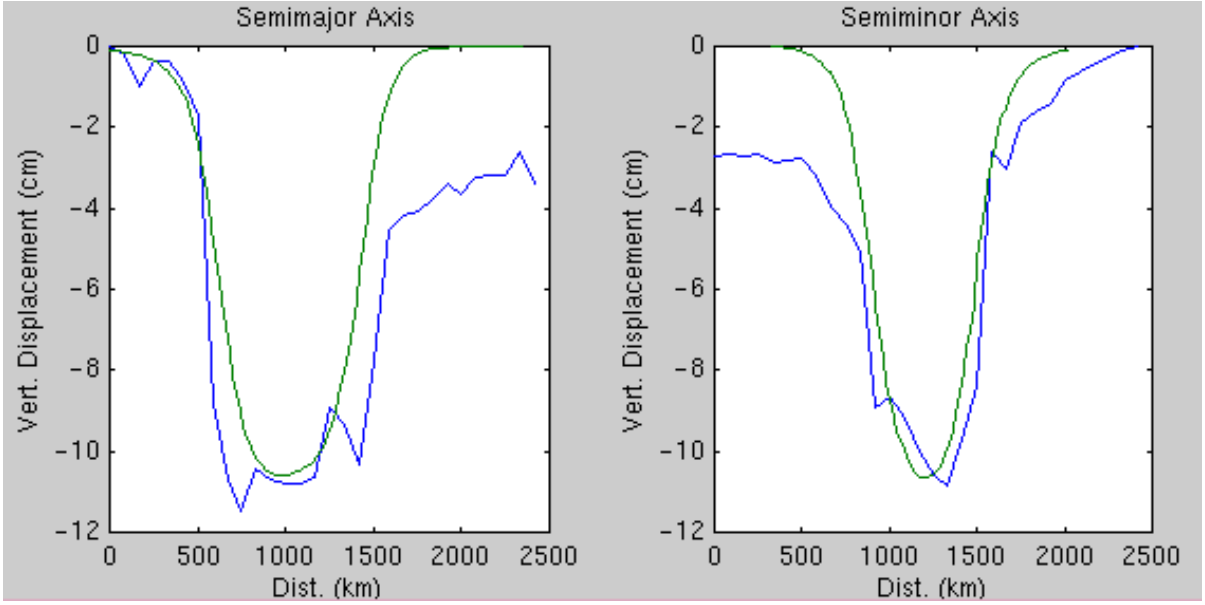

Figure 7. Comparison plots between model and data interferograms for source hypothesis #2 (see text).

Discussion and Conclusion

InSAR holds great promise in helping to identify and characterize shallow events under the CTBT. Shallow events include "false alarms" that that produce anomalous seismic signals, such as shallow earthquakes and the failure of underground cavities (e.g., mine collapses) that need to be distinguished from banned underground nuclear tests. In an effort to begin to understand the range of complex surface deformation signals possible from underground explosions, including complicating effects such as spall, post-event cavity collapse and cratering, we have begun to investigate the surface deformation produced by well studied U.S. nuclear tests at the Nevada Test Site. While we have not yet fully investigated all parameters surrounding these tests, and there is more site information to gather to better constrain our models, important conclusions can be drawn from this study that have important ramifications for CTBT verification efforts. The results presented here yield new information about the detectability of underground explosions and demonstrate that by using differential SAR interferometry in conjunction with established seismic detection methods the following may be obtained:

1) Possible identification of underground explosions *after* they happen with no need for a "before" image.
2) Locations of suspect events to within a hundred meters. This is true even for fully contained tests that do not crater and that have no visible surface traces.
3) The dimensions, shape and amount of surface deformation associated with an event.

An important caveat to these findings are that event JUNCTION was a relatively large m_b=5.6 event and this is most likely the reason that it can be detected and characterized using differential InSAR. Although decorrelation and orbital phase flattening problems may have obscured the smaller events in our interferograms, the detection of smaller test events including the NPE chemical explosion event appears to be much more difficult. However, we are optimistic that we will be able to improve the signal-to-noise ratio of our images, acquire additional data and begin to capture some of these smaller test events in future interferograms. We are confident that we will be able to gain significant additional information such as independent estimates of source depth, yield and the presence or absence of large underground cavities by using a combination of seismic and InSAR methods.

REFERENCES

Ellis, W.L., and R.P. Snyder, Asymmetry of collapse sinks in Yucca Flat, Nevada Test Site, Nevada, Report USGS-474-180 prepared by the U.S. Geological Survey, Denver, for the U.S. Atomic Energy Commission, Nevada Operations Office, 20 p., 1974.

Foxall, B., J.J. Sweeney, W. R. Walter, Identification of Mine Collapses, Explosions and Earthquakes using INSAR: A Preliminary Investigation, , 1998.

Goldstein, R.M., Zebker, H.A., Werner, C.L., Satellite Radar Interferometry: Two dimensional Phase Unwrapping, Radio Science, 23, No. 4, 1988.

Murphy, J., Types of seismic events and their source descriptions, in Monitoring a Comprehensive Test Ban Treaty, editors E. S. Husebye and A. M. Dainty, Kluwer Academic Publishers, Dordrecht, 225-246. 1996.

Rosen, P.A., C. Werner, E. Fielding, S. Hensley, S. Buckley, P. Vincent, Aseismic creep along the San Andreas fault northwest of Parkfield, CA, measured by radar interferometry, Geophys. Res. Lett., 25, 825-228, 1998.

Terhune, R.W., and H.D. Glenn, Estimate of Earth media shear strength at the Nevada Test Site, UCRL- 52358, Lawrence Livermore National Lab., 29 p., 1977.

Vincent, P., J.B. Rundle, J. Fernandez, S.M. Buckley, SAR-constrained models of coseismic and interseismic deformation, EOS trans., AGU, 78, 46, 1997.

Vincent, P., Application of SAR Interferometry to Low-Rate Crustal Deformation Fields, Ph.D. Thesis, University of Colorado, 1998.

Vincent, P., J.B. Rundle, R. Bilham, S.M. Buckley, Aseismic creep along the San Andreas and Superstition Hills faults with uplift at Durmid Hill, southernmost San Andreas fault, CA measured by radar interferometry, EOS trans., AGU, 79, 45, 1998.